Solar Physics (2005) 226: 73–95

ELECTRON ACCELERATION IN RECONNECTING CURRENT SHEETS

PAUL WOOD and THOMAS NEUKIRCH
School of Mathematics and Statistics, University of St. Andrews, St. Andrews, KY16 9SS, U.K.
(e-mail: paul@mcs.st-and.ac.uk; thomas@mcs.st-and.ac.uk)

(Received 20 September 2004; accepted 22 October 2004)

Abstract. We present the results of charged particle orbit calculations in prescribed electric and magnetic fields motivated by magnetic reconnection models. Due to the presence of a strong guide field, the particle orbits can be calculated in the guiding centre approximation. The electromagnetic fields are chosen to resemble a reconnecting magnetic current sheet with a localised reconnection region. An initially Maxwellian distribution function in the inflow region can develop a beam-like component in the outflow region. Possible implications of these findings for acceleration scenarios in solar flares will be discussed.

1. Introduction

The acceleration of huge numbers of charged particles to high energies in solar flares is still very much an unsolved problem. Many different mechanisms have been proposed but none can as yet explain all of the observational signatures in a satisfactory way.

Apart from radio observations which can be made from the ground, the most important signatures of high energy solar flare particles occur at X-ray and gamma-ray wavelengths. As observations at these wavelengths can only be made outside the Earth's atmosphere, space missions like *Yohkoh* and the Compton Gamma Ray Observatory (CGRO) have been essential in providing us with data of solar flares. The RHESSI mission, launched in 2002, is dedicated to high-energy solar events and has greatly improved observations of accelerated particle signatures at X-ray and gamma-ray wavelengths by combining imaging capabilities with high spectral resolution right up into the MeV range. First results already show surprising details, e.g. in one flare gamma-ray sources of accelerated protons did not coincide with hard X-ray electron sources (Hurford *et al.*, 2003). For more comprehensive reviews of the (pre-RHESSI) observations and a concise summary of the main constraints facing any theory of particle acceleration in solar flares we refer to Miller *et al.* (1997) and Aschwanden (2002).

It is generally accepted that the energy released in a flare is previously stored in the magnetic field, and that the release process involves magnetic reconnection at some stage. Direct acceleration by the reconnection electric field is therefore one possible mechanism for the generation of high-energy particles during solar

flares, and in the present paper we will focus exclusively on direct electric field acceleration. In general, we expect that several different acceleration mechanisms will be at work either simultaneously or sequentially during solar flares.

Apart from direct acceleration, it has also been suggested that magnetic reconnection could cause particles to be accelerated by turbulent magnetic fields in the reconnection outflow (e.g. Moore, LaRosa, and Orwig, 1995; LaRosa *et al*., 1996) or by the inductive field caused by the shrinkage of field lines having undergone reconnection (collapsing trap model; Somov and Kosugi, 1997; Karlický and Kosugi, 2004). Another suggestion was that the interaction of the fast reconnection outflow with the stronger magnetic field in the lower corona can lead to the formation of a fast-mode shock (Somov and Kosugi, 1997; Tsuneta and Naito, 1998) which could in turn accelerate particles.

Not directly connected to the magnetic reconnection process are acceleration models based on stochastic acceleration (e.g. Miller and Roberts, 1995; Miller, LaRosa, and Moore, 1996; Lenters and Miller, 1998) of particles in (small-amplitude) turbulent electromagnetic fields. In these models, it is generally assumed that the energy released during a flare is somehow deposited in the turbulent wave fields and is then transferred into particle energy by a diffusive process in momentum space. Compared with direct acceleration models, stochastic models usually lack spatial information, but are more detailed in terms of, e.g., the evolution of distribution functions of accelerated particle populations.

Direct electric field acceleration is usually studied in the framework of reconnecting current sheets (e.g. Martens, 1988; Martens and Young, 1990; Litvinenko and Somov, 1993; Litvinenko, 1996; Zharkova and Gordovskyy, 2004) or in X-point like configurations (e.g. Bulanov and Sasorov, 1976; Bruhwiler and Zweibel, 1992; Fletcher and Petkaki, 1997; Browning and Vekstein, 2001; Litvinenko and Craig, 2000; Craig and Litvinenko, 2002; Heerikhuisen, Litvinenko, and Craig, 2002). In such studies, the electric and magnetic fields are usually assumed to be independent of time and have a simple dependence on the spatial coordinates. In particular, a spatially constant electric field is normally imposed, either by assumption or as a consequence of stationarity and an assumed spatial invariance. Exceptions are studies which use fields from MHD simulations (e.g., Kliem, 1994) or time-dependent solutions of the linearized MHD equations (e.g., Petkaki and Mackinnon, 1997; Hamilton *et al*., 2003). The acceleration of charged particles is then investigated by studying the particle orbits in the given electromagnetic fields.

This method has not only been applied to solar flares, but also to other astrophysical phenomena, e.g the acceleration of particles to ultra-relativistic energies in active galactic nuclei and jets (e.g. Schopper, Birk, and Lesch, 1999; Nodes *et al*., 2003). It is interesting to compare these studies with those of solar flares, even though the different parameter regimes do not necessarily allow for a direct application of the results to the Sun. For example, the radiation reaction force or the interaction of the particles with the energetic photons of a background radiation field are negligible in the solar case.

Magnetic reconnection is generically associated with a localised magnetic field-aligned component of the electric field caused by the violation of the ideal Ohm's law (e.g. Hesse and Schindler, 1988; Schindler, Hesse, and Birn, 1991; Hesse, 1995). This localization of the electric field component parallel to the magnetic field is not included in the models of reconnecting current sheets or X-points mentioned earlier. It is one of the objectives of the present paper to generalize the previous models to include a spatially varying field-aligned component of the electric field which drops to zero outside the reconnection region.

We also aim at combining the pictures of reconnecting current sheet and X-point configurations and study a current sheet configuration containing an X-point. For simplicity, we will assume that our fields are spatially invariant in one direction. Since we expect the particle acceleration time scale to be much shorter than the MHD time scale, we will also assume that the electromagnetic fields do not change over the time scales we consider. This is not the same as suggesting that the fields are static. Therefore, any electric field in this paper should be considered as an inductive field and not as a potential field.

Following Litvinenko (1996), we assume the presence of a strong magnetic field component in the invariant direction. This allows us to use the guiding centre approximation for the particle orbits. Under the assumption of collisionless transport, we investigate in detail how a Maxwellian distribution in the reconnection inflow region is modified by the electromagnetic fields, in particular the dependence of the energy distribution function on position in the reconnection outflow region.

We would like to emphasize that we have not attempted to carry out a self-consistent investigation. The electromagnetic fields used in the present paper have been chosen in such a way that they on the one hand give a reasonable representation of fields in and around regions undergoing magnetic reconnection, but on the other hand are still simple enough to allow for a largely analytical treatment. The particles are treated in the sense of non-relativistic test particles and no back reaction of the particles onto the fields has been taken into account. A fully self-consistent treatment would require Vlasov or particle-in-cell simulations. Although considerable progress has been made over the past few years (e.g., Hesse, Kuznetsova, and Hoshino, 2002; Drake *et al.*, 2003; Ricci, Lapenta, and Brackbill, 2003; Pritchett and Coroniti, 2004), a fully self-consistent treatment of a comparable problem still seems to be too ambitious.

The paper is organized as follows. In Section 2 we describe in detail how we determine the electromagnetic fields we use. In Section 3 we give the equations of motion we solve and describe how we calculate the particle distribution functions in the outflow region. Section 4 gives the results of our calculations and discusses the dependence of those results on model parameters like maximum electric field strength or the dimensions of the dissipative region. Finally, Section 5 gives a detailed discussion of the results and conclusions.

2. The Electromagnetic Fields

Our aim is to study the acceleration of charged particles in electromagnetic fields which mimic the fields occurring during the reconnection phase of a solar flare. Previous work has concentrated on either current sheet or X-point configurations. In the present contribution, we will aim to combine these two configurations by assuming an overall current sheet configuration with an embedded X-point. The X-point marks the centre of the non-ideal region which allows magnetic reconnection to occur. The magnetic field is completed by a strong field component perpendicular to the current sheet/X-point configuration. This guide field has the effect of increasing the period of time for which particles stay inside the reconnection region in which they feel strong accelerating electric field (e.g. Litvinenko, 1996). We will assume that for electrons the guide field is strong enough to guarantee that the guiding centre approximation can be used to calculate the particle orbits. As in previous papers on this subject (Bruhwiler and Zweibel, 1992; Litvinenko, 1996; Browning and Vekstein, 2001), the field configuration used in the present paper is invariant in one direction (the z-direction).

2.1. The magnetic field

To ensure $\nabla \cdot \mathbf{B} = 0$ we write the magnetic field in the form

$$\mathbf{B} = \nabla A \times \hat{\mathbf{z}} + B_z \hat{\mathbf{z}}. \tag{1}$$

Here $A(x, y)$ is the magnetic flux function and we assume that $B_z = B_0$ is the constant magnitude of the guide field.

Normalizing the magnetic field with respect to the guide field B_0, we assume that the flux function is given by

$$A(x, y) = \lambda \ln[\cosh(y) + e^{(-x^2/L^2)}]. \tag{2}$$

The corresponding magnetic field has the structure of a Harris sheet (Harris, 1962) for large $|x|$ or $|y|$, but contains an X-point at $x = y = 0$ (see Figure 1).

As already stated, we have assumed that the magnetic field in the x–y plane has been normalised to the value of the z-component of the field, so $\lambda = B_{x\infty}/B_0$, where $B_{x\infty}$ is the value of B_x in the limit $|y| \to \infty$ and B_0 is the value of the guide field. In normalised units, the amplitude of the guide field is therefore equal to one. In our standard case, the value of B_0 will be assumed to be 50 G and $\lambda = 1$, but the results can of course be scaled by an appropriate factor since we use dimensionless equations. The components of the dimensionless magnetic field are given by

$$B_x = \lambda \frac{\sinh y}{\cosh y + e^{(-x^2/L^2)}}, \tag{3}$$

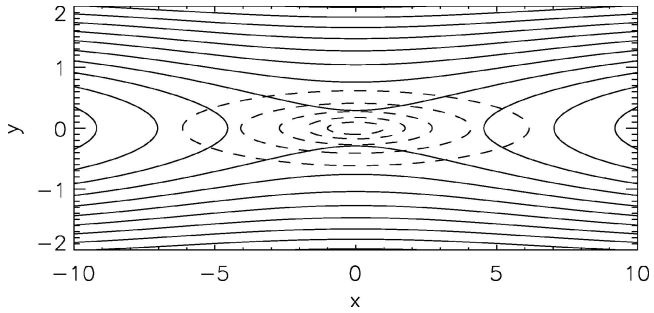

Figure 1. An example of the field configuration used in this paper (using $L = 10$). Note that for graphical reasons the configuration is not shown with the correct aspect ratio, so that it is actually a lot more elongated in the x-direction than shown here. The *solid lines* are projections of magnetic field lines onto the x–y plane (contours of the flux function A). The non-ideal region in which a field-aligned component of the electric field exists is outlined by the *dashed contours*.

$$B_y = \frac{2\lambda}{L^2} \frac{x e^{(-x^2/L^2)}}{\cosh y + e^{(-x^2/L^2)}}, \tag{4}$$

$$B_z = 1.0. \tag{5}$$

Length scales have been normalized in such a way that the current sheet half-width $L_{\rm cs}$ is one, and L represents the extension of the X-type region of magnetic field in the y-direction measured in units of $L_{\rm cs}$. The actual value of $L_{\rm cs}$ for current sheets in the solar corona is unknown observationally, but for example in MHD reconnection simulations (e.g. Zeiler *et al.*, 2002; Shay *et al.*, 2003) studying the formation of current sheets a typical sheet thickness is found to be about 10 ion inertial lengths ($10c/\omega_{pi}$, where ω_{pi} is the proton plasma frequency). For typical coronal conditions (particle density $n = 10^{15}$ m^{-3}) this is ≈ 70 m. However, Litvinenko (1996) uses a sheet half-width of 1 m, and later quotes a typical width of 10 m. For comparison, a typical electron Larmor radius using the thermal velocity for a temperature of $T = 2 \times 10^6$ K is $\approx 6.3 \times 10^{-3}$ m in a 50 G magnetic field. As it is still completely unclear what range of widths a reconnecting current sheet might have, we usually take 10 m as a reference width in our configuration. As we will operate with suitable non-dimensionalised equations, an increase or decrease of the reference width would increase or decrease the other length scales by the same factor.

A basic assumption of our model is that the time scale on which particles are accelerated is much shorter than the time scale on which the electric and magnetic field changes. We will therefore neglect any time dependence of the magnetic and electric fields and consider the fields as a snapshot being taken during their slow time evolution.

2.2. THE CURRENT DENSITY

We will need the current density **j** when we determine the electric field used in our model. In our normalization, the current density is given by

$$\mathbf{j} = \nabla \times \mathbf{B} = -\left(\frac{\partial^2 A}{\partial x^2} + \frac{\partial^2 A}{\partial y^2}\right)\hat{\mathbf{z}} = j_z \hat{\mathbf{z}}, \tag{6}$$

with

$$j_z = \lambda \frac{2e^{-x^2/L^2}/L^2\left[(1 - 2x^2/L^2)\cosh y + e^{-x^2/L^2}\right] - 1 - e^{-x^2/L^2}}{(\cosh y + e^{-x^2/L^2})^2}. \tag{7}$$

For large $|x|$, this current density tends to the Harris sheet current density $\mathbf{j} = -(\lambda/\cosh^2 y)\,\hat{\mathbf{z}}$ but for $x \simeq 0$ it behaves differently, due to the X-point structure.

2.3. THE ELECTRIC FIELD

The electric field used for our particle orbit calculations should resemble the electric fields known to be associated with magnetic reconnection. We emphasize, however, that we regard this purely as a motivation for our choice of electric field and that in the present paper we do not aim to find an electric field which satisfies all equations of kinematic or full MHD. We rather aim to find an electric field which captures the essential features of the electric field, in and around a reconnection region. In particular, we want the field-aligned component of the electric field to be localised, i.e., to go to zero quickly away from the reconnection region. This allows a clear distinction between the parallel (field aligned) electric field usually thought to be responsible for particle acceleration and the perpendicular electric field associated with the bulk inflow and outflow of the reconnection region.

As a proxy for finding such an electric field, we use Ohm's law in the usual non-ideal MHD version,

$$\mathbf{E} = \eta \mathbf{j} - \mathbf{v} \times \mathbf{B}, \tag{8}$$

to determine an appropriate electric field (a similar approach has been taken by Zharkova and Gordovskyy, 2004). Here **v** represents the bulk flow velocity of plasma in and out of the reconnection region, and η the resistivity of the plasma.

The resistive $\eta\mathbf{j}$ term is responsible for the parallel (field-aligned) electric field component, whereas the $\mathbf{v} \times \mathbf{B}$ term represents the perpendicular electric field component due to plasma convection.

The localization of the current density in the y-direction automatically causes a localization of the parallel electric field in y, but there is no corresponding localization of $E_\parallel$ in the x-direction. We achieve this localization by making the resistivity space dependent, similar to resistive MHD simulations (e.g., Schopper, Birk, and

Lesch, 1999; Nodes *et al.*, 2003):

$$\eta(x, y) = \frac{\eta_0}{\cosh^2(x/L_{\eta x})\cosh^2(y/L_{\eta y})}, \tag{9}$$

where the length scales $L_{\eta x}$ and $L_{\eta y}$ allow for the possibility of choosing the variation of η in x and y separately from each other, and also to change these length scales with respect to the length scale of the magnetic field. We will use this possibility to restrict the spatial extent of the parallel electric field. The constant η_0 influences the magnitude of the parallel electric field directly, and the value of η_0 is chosen to fix the maximum value of the parallel electric field at $x = y = 0$ given by

$$E_0 = E_z(0, 0) = \eta_0\, j_z(0, 0) = \eta_0\, \lambda \left(\frac{1}{L^2} - \frac{1}{2}\right). \tag{10}$$

We will usually choose this value of E_0 to be comparable to previous work (e.g., Litvinenko, 1996 uses a value of 10 V cm^{-1}), but we will also carry out calculations with a lower maximum value of the electric field. We would like to emphasise again that we are considering Ohm's law only as a proxy for determining a reasonable electric field configuration. An example of the resulting localised parallel electric field is shown in Figure 1 using dashed contours.

The components of the electric field perpendicular to the magnetic field are determined by the flow field **v**. Consistent with the two-dimensional nature of the magnetic field, we choose the flow field to have only x- and y-components. In agreement with the usual reconnection theory for two-dimensional fields plus guide field component, we assume that the flow is incompressible, i.e.,

$$\mathbf{v} = \nabla\psi \times \hat{\mathbf{z}}. \tag{11}$$

We choose the stream function ψ to have the form

$$\psi = v_{y\infty} L_{vx} \tanh(x/L_{vx}) \tanh(y/L_{vy}). \tag{12}$$

The corresponding velocity field $\mathbf{v}_{\text{flow}}$ has components

$$v_{\text{flow},x} = v_{y\infty} \frac{L_{vx}}{L_{vy}} \frac{\tanh(x/L_{vx})}{\cosh^2(y/L_{vy})}, \tag{13}$$

$$v_{\text{flow},y} = -v_{y\infty} \frac{\tanh(y/L_{vy})}{\cosh^2(x/L_{vx})}. \tag{14}$$

The velocity field has a stagnation point at the magnetic X-point, with inflow localised around the y-axis and outflow localised around the x-axis. The flow speed in both directions has a finite asymptotic value. The asymptotic value of the flow speed in the y-direction is given by $v_{y\infty}$. The corresponding value in the x-direction differs by the ratio of the length scales L_{vx}/L_{vy}. In the present paper, we assume that $L_{vx} = L$ and $L_{vy} = 1$, i.e. that the flow field varies on the same length scales

as the magnetic field. Since L is larger than 1 in the current sheet configurations used by us, we automatically get a slow inflow and fast outflow, with the asymptotic outflow velocity being a factor L faster than the inflow velocity. This is consistent with the usual view that magnetic reconnection causes an accelerated outflow from the reconnection region.

The magnitude of the flow velocity is a free parameter of our model. We fix this parameter by assuming that the asymptotic outflow speed is a few tenths of the coronal Alfvén velocity, consistent with many reconnection models. The inflow speed then follows according to the ratio of the length scales of the flow. We regard an outflow speed of 300 km s^{-1} as typical, corresponding to a coronal Alfvén speed of about 1000 km s^{-1}. We emphasize again that we will use dimensionless quantities throughout so that appropriately scaled speeds are possible. The major quantity needed for our calculations is the resulting perpendicular component of the electric field, the flow field is only a proxy for calculating this part of the electric field and thus only of secondary importance.

2.4. Summary

We briefly summarise here the approach we have taken and how well our assumed field satisfies the MHD equations. Our **B** field is a modified Harris sheet with an X-point in the centre. Our parallel electric field is restricted to the region around the X-point. This choice of **E** is the principle difference between our work and recent studies (e.g., Litvinenko, 1996; Browning and Vekstein, 2001), who take a constant $E = E_0\,\hat{\mathbf{z}}$. This choice implies that $\nabla \times \mathbf{E}$ is non-zero. This is deliberate since we view this configuration as a snapshot of an inductive field, but we ignore the time dependence of B, assuming that the electron acceleration time scale is much shorter than the MHD time scale.

In our configuration, A satisfies the Grad–Shafranov equation only approximately, since it is close to the A of a Harris sheet. The velocity field v_{flow} is a stagnation flow ensuring $\nabla \cdot \mathbf{v} = 0$, with inflow and outflow velocities not inconsistent with the general theoretical picture of reconnecting current sheets (e.g., Priest and Forbes, 2000). We emphasise once again that some assumptions have been made in order to create a reasonably simple model that captures the essential features of an X-type current sheet.

3. The Particle Equations of Motion

The electromagnetic fields of the previous section are used to calculate the orbits of electrons within these fields, in particular to study the acceleration of electrons in these fields. In the present paper, we find that some particles reach mildly relativistic energies (up to 500 keV) but very few reach such values so we have chosen to use

the nonrelativistic equations of motion, given by

$$m_e \frac{d^2\mathbf{r}}{dt^2} = -e\left[\mathbf{E} + \frac{d\mathbf{r}}{dt} \times \mathbf{B}\right], \tag{15}$$

where $\mathbf{r}(t)$ is the position of the particle at time t, m_e the electron mass, and e the elementary charge.

Due to the guide field component included in our model magnetic field, the electron motion can always be regarded as a combination of a guiding centre drift and a gyrational motion. Because the gyrational motion happens on much smaller spatial and time scales than the drift motion, it will limit the size of the time step in any numerical method used to solve Equation (15) and increase the amount of computing time needed dramatically.

It is therefore much more convenient to use the guiding centre or drift approximation to calculate the electron trajectories. With the electromagnetic fields given in Section 2, the guiding centre theory provides us with an excellent approximation to the true electron orbits, but avoids the limitations on the time steps of full orbit methods.

In the guiding centre approximation, the true position of the particle $\mathbf{r}(t)$ is approximated by the guiding centre position $\mathbf{R}(t)$, which is the centre of the instantaneous gyrational motion. The particle velocity is split into a gyrational component and drift component. The drift component is given by the time derivative of the guiding centre position $\mathbf{R}(t)$, whereas the gyrational component only appears in the magnetic moment $\mu = m_e v_\perp^2/2B$, which is an adiabatic invariant. To calculate the electron trajectories within the guiding centre approximation, we use the equations as given by Northrop (1963). We use the same normalisation as given earlier (length scales normalised to the current sheet half-width L_{cs}, magnetic fields to the value of the constant guide field B_0, electric fields to the value of E_z at $x = y = 0$, E_0), but in addition we normalise velocities by E_0/B_0 and time by $L_{cs}B_0/E_0$. With this normalisation, the guiding centre equations take the form

$$\frac{dv_\parallel}{dt} = -\frac{1}{\varepsilon} E_\parallel - \mu \frac{\partial B}{\partial s} + \mathbf{u}_E \cdot \left[\frac{\partial \mathbf{b}}{\partial t} + v_\parallel \frac{\partial \mathbf{b}}{\partial s} + (\mathbf{u}_E \cdot \nabla)\,\mathbf{b}\right], \tag{16}$$

$$\frac{d\mathbf{R}}{dt} = \mathbf{u}_E + v_\parallel \mathbf{b} - \varepsilon \left\{\mu \frac{\mathbf{B} \times \nabla B}{B^2} - \frac{\mathbf{B}}{B^2} \times \left[v_\parallel \frac{\partial \mathbf{b}}{\partial t} + v_\parallel^2 \frac{\partial \mathbf{b}}{\partial s} + v_\parallel (\mathbf{u}_E \cdot \nabla)\mathbf{b} + \right.\right.$$

$$\left.\left. + \frac{\partial \mathbf{u}_E}{\partial t} + v_\parallel \frac{\partial \mathbf{u}_E}{\partial s} + (\mathbf{u}_E \cdot \nabla)\mathbf{u}_E\right]\right\}, \tag{17}$$

where

$$\mathbf{b} = \frac{\mathbf{B}}{|B|}, \tag{18}$$

$$\frac{\partial B}{\partial s} = (\mathbf{b} \cdot \nabla)B, \tag{19}$$

$$\mathbf{u}_E = \frac{\mathbf{E} \times \mathbf{B}}{B^2}. \tag{20}$$

According to our approximation of the evolution of the electromagnetic fields, we neglect the terms containing time derivatives.

Equations (16) and (17) contain one dimensionless parameter ε, defined by

$$\varepsilon = \frac{m_\mathrm{e} E_0}{e B_0^2 L_\mathrm{cs}} = \frac{1}{\omega_{\mathrm{e,g}} T}. \tag{21}$$

Here $\omega_{\mathrm{e,g}}$ is the electron gyrofrequency in the guide field B_0 and T is time scale defined by $L_\mathrm{cs} B_0 / E_0$, which can be interpreted as an $\mathbf{E} \times \mathbf{B}$-drift time across one current sheet half-width L_cs (note, however, that E_0 is the value of the parallel electric field at the X-point and that B_0 is the value of the guide field). Since we assume the drift approximation to be valid we expect that the time scale defined by the gyrofrequency is much smaller than the drift time scale, and thus ε should be small. Indeed, if we rewrite ε using typical values for the various quantities it is defined by, we get

$$\varepsilon = 5.686 \times 10^{-2} \left[\frac{L_\mathrm{cs}}{\mathrm{m}}\right]^{-1} \left[\frac{B_0}{\mathrm{G}}\right]^{-2} \left[\frac{E_0}{\mathrm{V\,cm^{-1}}}\right]. \tag{22}$$

For our standard values $L_\mathrm{cs} = 10$ m, $B_0 = 50$ G and $E_0 = 10$ V cm^{-1} one obtains $\varepsilon \approx 2.275 \times 10^{-5}$. Therefore, in Equation (16) the first term will be dominant where $E_\parallel$ is of any noticeable strength (i.e., inside the reconnection region). In Equation (17), the first two terms ($\mathbf{E} \times \mathbf{B}$-drift and guiding centre motion along the field) will be the most important terms, but we include all terms in our calculations.

The guiding centre approximation remains valid as long as changes in the magnetic field are on time and length scales much bigger than the gyroradius and period. Without B_z, particles have meander orbits near the magnetic null point, but the addition of a strong guide field ensures it remains valid in the whole domain of study.

3.1. Particle distribution functions

To simulate a population of particles with different initial conditions, we start our guiding centre calculations at a fixed position $y = y_\mathrm{in}$ outside the current sheet. The configuration is invariant in z so we need only vary x to simulate different initial positions. Since we are using the guiding centre approximation, we have less freedom than in a full particle orbit calculation regarding the initial (guiding centre) velocity (note that Equations (16) and (17) are only four first-order differential equations corresponding to four independent initial conditions, whereas the full equations of motion require six initial conditions). Thus, we can only prescribe $v_\parallel$

in addition to the initial position. However, the value of the magnetic moment μ can also be varied for different orbits, but as μ is a constant of motion, strictly speaking it is not to be regarded as an initial condition.

To model a coronal particle population, we assume that at each initial position the particles have a Maxwellian energy distribution and that the particle density is the same for each initial position. The initial particle distribution function is then given by

$$f(x, v_\parallel, \mu) = f_0 \exp\left(-\frac{m_e v_\parallel^2 + 2\mu B}{2k_B T}\right). \tag{23}$$

Assuming a coronal temperature of 2×10^6 K the electron thermal speed ($\sqrt{k_B T/m_e}$) is $\approx 5.5 \times 10^3$ km s^{-1} (measured in units of our velocity normalisation, the thermal speed is $\approx 5.5[E_0/(\mathrm{V\,cm^{-1}})]^{-1}[B_0/\mathrm{G}]$).

Over the time and length scales considered here the corona is largely collisionless, and so the value of the particle distribution function stays constant along particle orbits. We therefore transport the value of the distribution function along calculated particle orbits and construct a final distribution function in the reconnection outflow region (at constant $x = x_{\mathrm{out}}$).

The initial conditions for the particle orbits are determined as follows. In x we take 200 initial values spread uniformly across the length of the current sheet. In velocity space, we sample the parallel velocity up to about four times the thermal velocity in both positive and negative directions with a total 340 different values for the initial $v_\parallel$. For each x and each $v_\parallel$ value, we calculate particle orbits for 170 different values of μ between 0 and ≈ 5000.[1] In total, each simulation involves about 10^7 particle orbits.

The orbits are classified according to the field lines on which they cross $x = x_{\mathrm{out}}$ and by their energy at that position. The position 'bins' are created by separating particles according to final y position. It is then possible to create energy spectra for different positions in relation to the projected separatrix field lines. For better comparison with the observations, the energy spectra for the different cases are usually created with 1 keV resolution, although some plots are created with a coarser resolution for smoothness. We remark that these energy values can be rescaled for different values of E_0 and B_0 (E_0' and B_0', say) by multiplying the energy values by the factor $(B_0/B_0')^2(E_0/E_0')^{-2}$, provided the value of the parameter ε is kept constant at the same time (if ε changes the particle orbits and thus the distribution function will change).

[1] In our normalisation, the electron Larmor radius for a given magnetic moment μ can be written as $r_{\mathrm{L}} \approx 8.04 \times 10^{-2}[E_0/\mathrm{V\,cm^{-1}}][B_0/\mathrm{G}]^{-2}\sqrt{\mu/B(x, y)}$ m. For our standard values $E_0 = 10$ V cm^{-1} and $B_0 = 50$ G, we obtain for $\mu = 5000$ and $B(x, y) = 1$ a Larmor radius of $\approx 2.3 \times 10^{-2}$ m, still a lot smaller than L_{cs}. This value is about twice the Larmor radius of an electron with $v_\perp = v_{\mathrm{thermal}}$ in a plasma of temperature 2×10^6 K.

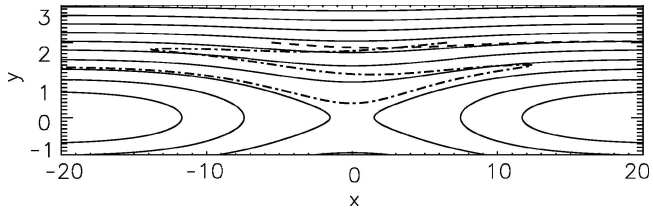

Figure 2. Two example particle trajectories (*dashed* and *dash-dotted lines*) superimposed onto projected magnetic field line contours.

4. Results

4.1. Typical trajectories

Due to the relatively strong guide field in our configuration the particles are strongly magnetized. As already briefly discussed in Section 3, the guiding centre motion consists of a perpendicular component mainly given by the dominant $\mathbf{E} \times \mathbf{B}$-drift and the field-aligned component. The $\mathbf{E} \times \mathbf{B}$-drift velocity is basically identical with the bulk flow field (Equations (13) and (14)) we have used as a proxy to determine a reasonable electric field in the ideal region. Without an area of enhanced resistivity all electron guiding centres would carry out this type of motion.

However, particles that pass close to the origin feel the effects of the parallel electric field and are strongly accelerated. Figure 2 shows examples of projections of two typical orbits onto the x–y plane. One orbit passes above the resistive region (dashed line), whereas the other one passes through it (dash-dotted line). The particular examples are chosen to represent the two basic, distinct types of motion. The parameter values of the electric and magnetic field used in this example are given in Table I.

TABLE I

Parameter values of electromagnetic field for orbits in Figure 2.

Parameter	Value
E_0	10 V cm^{-1}
B_0	50 G
λ	1
$L_{\rm cs}$	10 m
$L/L_{\rm cs}$	10
ε	2.275×10^{-5}
$L_{\eta x}/L_{\rm cs}$	1.666
$L_{\eta y}/L_{\rm cs}$	0.166

For the first trajectory, the initial conditions used were $x = -5.0$, $y = 2.0$, $v_{\parallel} = 10.0$ and $\mu = 500.0$. For this trajectory the gain in energy is negligible because it does not pass close enough to the resistive region to feel much of the parallel electric field.

In the other case, the initial conditions are $x = 6.5$, $y = 2.0$, $v_{\parallel} = -10.0$ and $\mu = 500.0$. The particle seems to feel some trapping effects as it bounces between the stronger field regions away from the X-point and is given a chance to drift right in towards the origin, receiving a much greater amount of energy. The example shown represents a gain in energy of around 50 keV. The particle leaves the sheet following field lines close to the separatrix (the field line coming directly from the X-point).

The highly restricted resistive region implies that the exact particle orbits are extremely sensitive to the initial parallel and perpendicular velocity. Energy gain is entirely dependent on how close the particle drifts to the X-point. Thus, the shape of the energy spectra can be expected to depend on the geometry of the current sheet.

In our orbit calculations the code stops when the trajectory reaches $30\,L_{\rm cs}$ in the x-direction (corresponding to 300 m if we use $L_{\rm cs} = 10$ m). Almost all the acceleration occurs in the first $10\,L_{\rm cs}$ in the x-direction. We run the code to $x = 30\,L_{\rm cs}$ to ensure that a particle has had the chance to gain maximum energy. The initial and final kinetic energies are calculated from the equation

$$E_{\rm kin} = \frac{1}{2} m v_{\parallel}^2 + \mu B \tag{24}$$

in our usual normalisation.

In the present paper, we only treat electrons since the values for the proton/ion Larmor radii would generally not allow for the guiding centre approximation to be used. Since the question of separation of accelerated protons and electrons has recently attracted some attention (e.g. Hurford *et al.*, 2003; Zharkova and Gordovskyy, 2004) we nevertheless want to briefly discuss this issue here. In the ideal case, with no resistive region, there is hardly any separation of accelerated electrons and ions whatsoever, whereas in the presence of a large and spatially constant parallel electric field the separation of accelerated electrons and ions is total. However, Figure 2 highlights the more complicated motion in a hybrid model like ours. It is possible for particles to exit the sheet in all four corners but the effect of the $E_{\parallel}$ in the non-ideal region will be to separate the accelerated electrons and ions. Since there is a gradual boundary between the ideal and resistive regions this separation will be extremely complex but confined to only the accelerated particles.

We also remark that in a self-consistent treatment of the acceleration process any tendency for charge separation would be accompanied by a strong modification of the electric field the consequences of which are difficult to assess. We would therefore like to re-emphasise that any results purely based on test particle calculations like ours are useful but should not be over interpreted.

4.2. EVOLUTION OF PARTICLE DISTRIBUTIONS

To construct a full sample of initial conditions for a current sheet with the parameters listed in Table I, we took a range of values for the initial position along the length of the sheet (x_0). The invariance in z of our model allowed us to set $z_0 = 0$ throughout, and we used $y_0 = 2\,L_{\rm cs}$, corresponding to particles drifting in from the top of the sheet as it is shown in Figure 1. We need only consider the positive value of y_0 since the symmetry of the model implies that the energy spectra will be the same above and below the X-point.

Combining these initial conditions with the distribution function in velocity space discussed earlier, we calculated the orbits of around 10^7 particles. The total final energy spectrum is shown as a double logarithmic plot in Figure 3. From the plot we see that obviously a vast majority of particles receive little or no acceleration. These are the particles that do not pass near the X-point region (corresponding to particles with trajectories similar to the dashed line orbit in Figure 2). For energies above a couple of keV, the spectrum has a power-law shape ($E^{-\gamma}$) with an index of $\gamma \approx 1.5$. This value is certainly a little harder than most observations of flares (e.g., Holman *et al.*, 2003 finds values of $2.5 < \gamma < 3.5$). However, Lin, Mewaldt, and Hollebeke (1982) find values of $\gamma \approx 1.5$ for the part of the spectrum between 10 and 100 keV in many flares. Our γ is comparable to the value predicted by Heerikhuisen, Litvinenko, and Craig, 2002. The spectrum could be softened by the inclusion of energy loss mechanisms or by a different choice of parameters.

The power law extends all the way up to around 500 keV, where the non-relativistic approximation is certainly no longer accurate. However, only such a

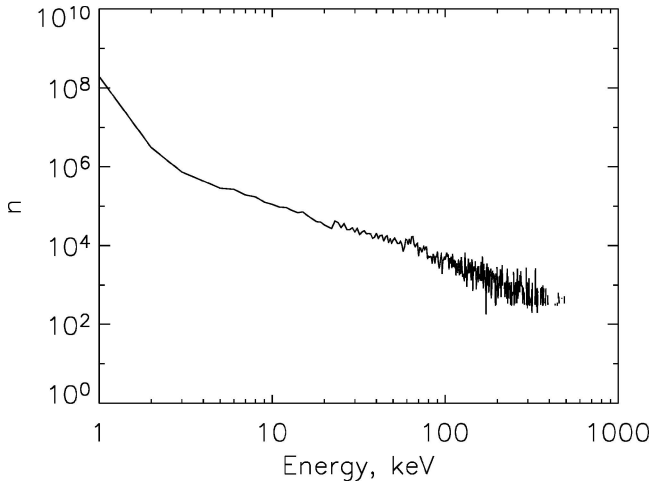

Figure 3. Double logarithmic plot of final energy spectrum using an initially Maxwellian particle distribution function. The initial position in x ranges from $-5\,L_{\rm cs}$ to $5\,L_{\rm cs}$. For the parameters given in Table I the bin width is 1 keV.

small number of electrons reaches these energies that this is not of too great concern. The plot highlights the following facts:

1. Energy gains of the right order of magnitude for flares are possible in our current sheet configuration.
2. The total final energy distribution is of a power-law shape for energies above ≈ 2 keV with a power-law index which is not a huge amount harder than observations.

Figure 4 shows two examples of electron spectra, grouped according to the value of y as they reach the sampling position $x = 30\,L_{\rm cs}$. This means that particles are collected into groups according to the field lines along which they are moving away from the X-point region. The two examples shown are from around the separatrix field line above and below the X-point. It is clear that a smaller number of particles passes below the X-point from above, and also that these two groups of field lines account for all of the accelerated particles. The huge bulk of thermal particles does not appear in these plots – they are spread across the whole range of field lines. Again, the energy distributions roughly follow power laws, with the lower separatrix distribution being slightly more ragged and showing a depletion of particles at low energies. The distribution is also flatter for the lower separatrix position.

Figure 5 shows an example where we use a finer resolution for the y 'bins'. The four examples shown are from just above the separatrix field line above the X-point. The most accelerated particles are found next to the separatrix field line with less energetic particles found in consecutive particle bins further above the separatrix. A calculation with a lower maximum electric field (and therefore lower maximum energy gain) was used to create Figure 5 because it shows the effect most clearly. It is obvious that a clearly defined bi-directional beam of energetic electrons has been created.

If we would use even finer resolution (i.e., smaller bin size), the particles can be sorted extremely accurately into energy bands by tracking which field lines they leave the box along. The most energetic particles are always found very close to

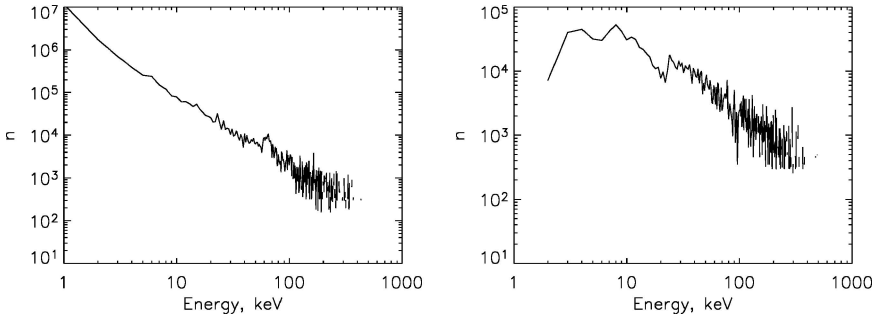

Figure 4. Left: Energy spectrum of particles collected next to the separatrix field line above the X-point. *Right:* Energy spectrum from next to the separatrix below the X-point.

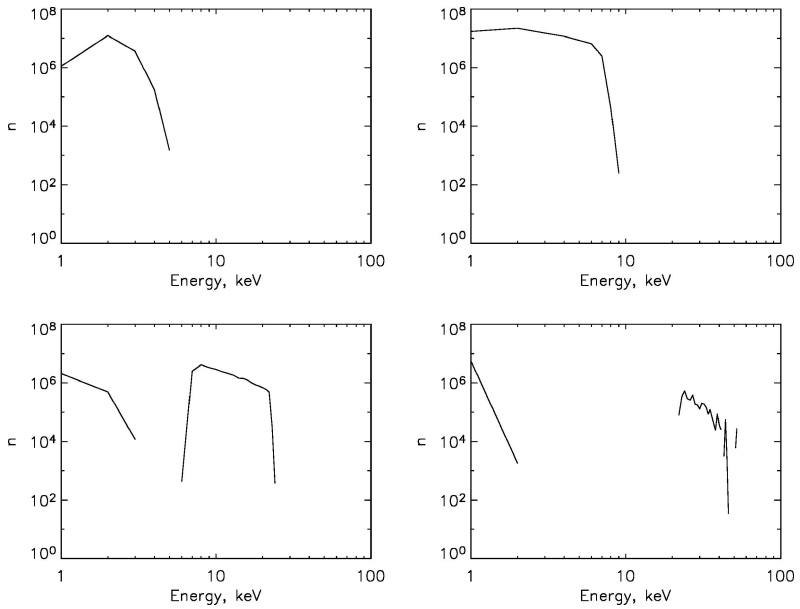

Figure 5. Each graph shows a double logarithmic plot of the energy spectrum for a particular y_{final} 'bin'. The *bottom-right graph* is the spectrum from field lines next to the separatrix above the X-point, while *bottom-left*, *top-right* and *top-left* are consecutive bins progressively further from the separatrix. The energy gains are smaller than in Figure 3 because we use a smaller maximum electric field to show the effect as clearly as possible. It is obvious that particular bands of energy have been partitioned according to the field lines along which they leave the current sheet. The bottom-right bin contains all of the particles that reach such high energies in the entire simulation (in addition to the corresponding bin below the X-point).

the separatrices, with lower energies always found successively further from these field lines.

4.3. VARIATION OF THE BASIC PARAMETERS

We look now at the sensitivity of these results with respect to changes of the current sheet parameters and/or initial conditions.

We therefore calculated energy spectra for a variety of initial spatial conditions. As the model has z-invariance, the z_0 value makes no difference and a change of y_0 to values larger than 2 will not change the results as particles will just drift into the current sheet from greater distance without gain in energy. Therefore, we vary only x_0. Taking a range from $-10\,L_{\text{cs}}$ to 0 instead of $-5\,L_{\text{cs}}$ to $5\,L_{\text{cs}}$ in the principal run, we obtain an almost identical spectrum, with the exception of a few extra particles that reach energies higher than 500 keV. This corresponds to a few initial conditions that let the particle drift gradually towards the separatrix field line and follow it in towards the X-point. As stated earlier, altering the value of y_0 also has

little effect. When y_0 is closer to the non-ideal region, we see a slight enhancement of accelerated particles, which is a natural consequence of making it easier for particles to reach the dissipative region. We conclude that not unexpectedly the variation in initial position does not significantly change the previous results.

The parameter about which observations tell us the least is the parallel electric field E_0. Foukal and Behr (1995) calculate an estimate of an upper limit on the electric field in a particular flare to be $\approx$35 V cm^{-1} using the Stark effect, while Martens (1988) argued that the effective resistivity in a reconnection region can be up to 5 orders of magnitude higher than the classical Spitzer value, giving rise to a parallel field strength similar to the 10 V cm^{-1} we use. The maximum size of the parallel electric field has a direct influence on the energy gain. Figure 6 shows the effect of varying E_0 by 2 orders of magnitude. Since varying E_0 alters the parameter ε (see Equation (21)) the whole motion of the particle is changed. Not only is the possible energy gain reduced, but the spectrum is steepened. The value of γ is $\approx$2.6 for $E_0 = 1.0$ V cm^{-1} and $\approx$4 for $E_0 = 0.1$ V cm^{-1}.

The spatial restriction of the resistive term can also be altered and Figure 7 shows an example of a less restricted parallel field with a maximum value of 0.05 V cm^{-1}. The parameter values are contained in Table II. The graph shows that maximum energy gains are increased by the less-restricted field (compared to the lower graph in Figure 6) but the energies are weaker than in Figure 3 due to the lower E_0. However, a much greater proportion of particles gain energy. The spectrum is much flatter and the huge bulk of particles in the lowest energy bin are not present. The clear bump in the spectrum just over 10 keV is a geometrical effect

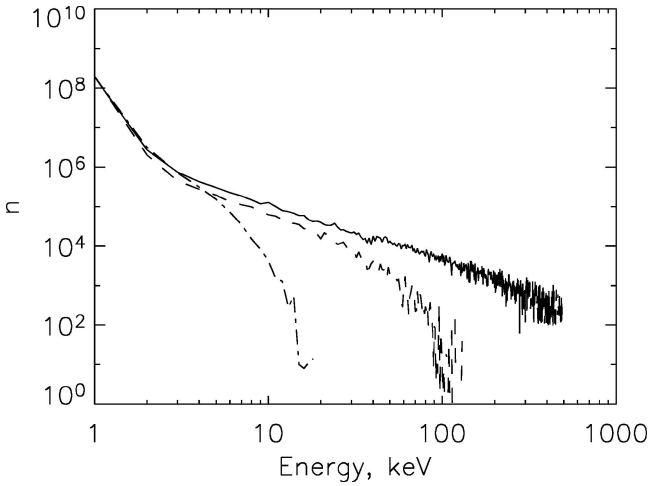

Figure 6. Energy spectra for a range of values of the maximum electric field, E_0. The *solid line* is the original spectrum ($E_0 = 10$ V cm^{-1}), the *dashed line* represents $E_0 = 1$ V cm^{-1} and the *dot-dashed line* $E_0 = 0.1$ V cm^{-1}. Apart from a clearly different maximum energy gain, the spectral index is steeper for lower E_0 values.

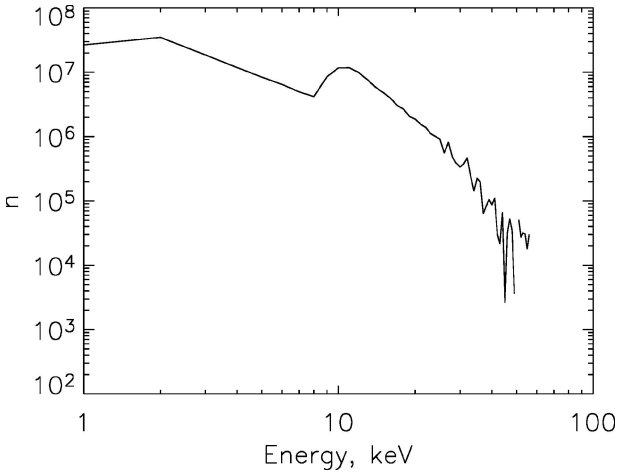

Figure 7. The energy spectrum obtained from a weaker, but more diffuse resistive region. The maximum value of E_0 is 0.05 V cm^{-1} but the area where resistivity is important is much larger than in the previous case.

TABLE II

Parameter values for a current sheet model with a weaker, but more extended E_0.

Parameter	Value
E_0	0.05 V cm^{-1}
B_0	50 G
λ	1
$L_{\rm cs}$	10 m
$L/L_{\rm cs}$	10
ε	1.138×10^{-7}
$L_{\eta x}/L_{\rm cs}$	10
$L_{\eta y}/L_{\rm cs}$	1

caused by the large number of electrons that pass below the X-point and receive acceleration on the way past.

4.4. Comparison with constant electric field model of Litvinenko

For comparison with our current sheet model, we have also carried out similar calculations for the fields used by Litvinenko (1996). Figure 8 shows the configuration (projected on the x–y plane) of the analytical reconnecting current sheet in

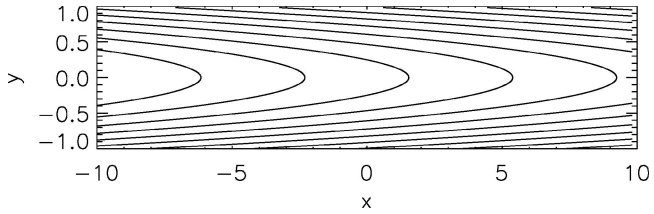

Figure 8. Magnetic field lines in the analytical reconnecting current sheet model of Litvinenko (1996).

Litvinenko (1996). B_z and E_z come out of the page. The electric field **E** and the magnetic field **B** are given by

$$\mathbf{B} = B_0(-y/a, \xi_\perp, \xi_\parallel), \tag{25}$$

$$\mathbf{E} = (0, 0, E_0). \tag{26}$$

The field is intended to model the inner part of a current sheet, given by the first terms of a Taylor expansion. The invariance in x means that it is sufficient in this configuration to study a single initial x-position. Figure 9 shows the energy spectrum created by a similar numerical method as given in the previous section, using the same distribution function in $v_\parallel$ and μ. The uniform energy gain in the sheet so far outweighs the initial variation in kinetic energy that the distribution function is almost mono-energetic. The energy gain agrees very well with the energy gain for particles that pass near to the origin in our model.

It is possible to obtain a broader energy distribution by considering particles with different initial values of y. This does not produce a power law though. In the paper, Litvinenko estimates a spectrum with $\gamma = 2$ if $B_\perp(x) \approx x$. Heerikhuisen, Litvinenko, and Craig (2002) use similar arguments to predict a power law with

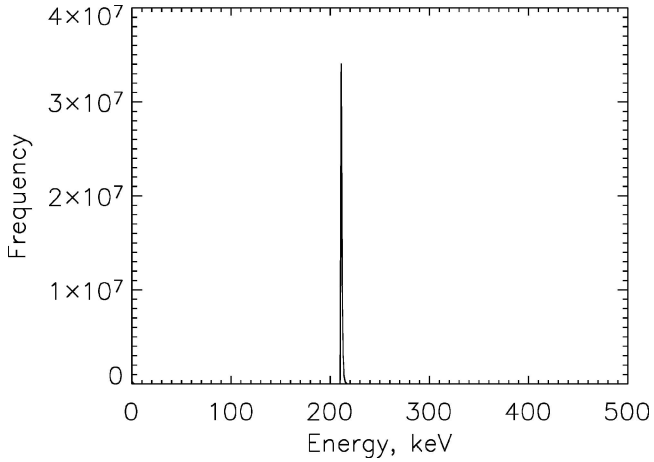

Figure 9. Energy spectrum produced by particles in the Litvinenko RCS.

$\gamma = 1.5$. Our numerical results agree well with both these estimates and Litvinenko's predicted energy gains of a few hundred keV.

The intention of the present paper is to combine a current sheet configuration à la Litvinenko (1996) with a spatially limited region of parallel electric field and to include a wider area outside the centre of the reconnection region. The comparison of the results highlights the gains to be made from this approach: more realistic energy spectra and bi-directional electron beams.

5. Discussion and Conclusions

Using the non-relativistic guiding centre equations of motion we have tracked the change in energy of Maxwellian distributions of electrons. This work can be thought of as a natural extension to previous work (e.g. Litvinenko, 1996; Browning and Vekstein, 2001). We have used a more "realistic" electromagnetic field configuration with a similar maximum of the electric field (10 V cm^{-1}) to find a power-law distribution of energy (with index $\approx$1.5) in the reconnection outflow region. The high-energy particles are concentrated around the separatrix field lines so that we get a beam-like spatial structure of the distribution function. In the case of a weaker maximum electric field we find both a reduction in the possible energy gains and a steepening of the spectrum while a less restricted resistive region has the effect of flattening the spectrum and particularly accelerating a great number of particles by a small ($<$20 keV) amount. In all these cases, the acceleration is entirely dependent on the geometry of the model. The closer a particle gets to the X-point, the more energy it receives.

We believe that there are a number of significant advantages to this type of model:

1. We have shown that it is possible to create power-law spectra which, while not quite consistent with observations, are encouragingly close to the harder part of broken power-law observations (e.g., Lin, Mewaldt, and Hollebeke, 1982 find $\gamma = 1.5$ for electrons up to $\approx$100 keV).
2. Bi-directional electron beams. The geometry of the model gives rise to equal numbers of accelerated electrons moving upwards and downwards (or left and right as our model is drawn).
3. Charge separation. The resistive region creates a partial separation of accelerated electrons and ions. The strength of the separation is dependent on the restriction of the parallel electric field. The field lines diverge on leaving the reconnection region, so even a small separation would be vastly amplified over the distance to the chromospheric footpoints. However, any conclusions about charge separation based on results which do not take the back reaction of the electric field into account should be regarded with caution.

4. The most energetic electrons collect along the separatrices. There is observational evidence (e.g. Metcalf *et al.*, 2003) that the locations of flare-associated chromospheric hard X-ray radiation are preferably aligned with the intersection of magnetic separatrix (or quasi-separatrix) surfaces with the chromosphere. This would be consistent with the fact that particle beams in our model leave the reconnection region along the separatrix field lines.

On the other hand, the major shortcoming of any reconnection dc field model is that the total number of accelerated particles is too small to solve the number problem (e.g., Miller *et al.*, 1997; Aschwanden, 2002). Assuming a typical active region coronal density of 10^{10} cm^{-3} and using the inflow rate of 30 km s^{-1} from our model we can work out the number of particles coming into the acceleration region around the X-point from both sides. Even if we assume limits of 10^7 m in the x- and z-direction the particle flux into the sheet would only be $\approx 6 \times 10^{34}$ s^{-1} (This would imply that we assume a continuous string of X-points over a range of 10 Mm. This sort of filamentary reconnection scenario has been suggested e.g. by Kliem (1994)). Furthermore, looking at the energy spectra only around 0.1% of the particles reach energies of 10 keV or above. In conclusion, the flux of electrons reaching energies over 10 keV is about 6×10^{31} s^{-1} for the optimistic assumption of length scales in x and z, a lot lower than the values required for a big flare which are of the order of at least 10^{35} s^{-1} (Miller *et al.*, 1997). We also mention that our model is of a two-dimensional nature and that we have not yet properly included the third dimension. Even though it is not entirely obvious how e.g. the distribution functions would change, it is intuitively clear that a restriction of the acceleration region (i.e. the region of parallel electric field) in the third direction limits the distance in z that the particles could be accelerated over and thus the possible energy gain. It will probably make the particle number problem worse, not better. The details will of course depend on the properties of a prospective three-dimensional model. We plan to investigate this question in the future.

There are various possibilities by which this shortfall in particle flux could be overcome, but all of these are outside the scope of this paper and are thus at the present time of a purely speculative nature. A number of numerical investigations using both MHD and kinetic theory show the tendency of the reconnection process to break up into several reconnection sites (e.g., Kliem, 1994; Kliem, Karlický, and Benz, 2000; Shay *et al.*, 2003) or to lead to secondary instabilities (e.g., Rogers, Drake, and Shay, 2000). In this limit the reconnection process would acquire a stochastic nature on large spatial and time scales, with an individual reconnection event probably looking similar to the process described in the present paper. Recent investigations of particle acceleration in reconnecting electromagnetic fields of stochastic type have been carried out by Vlahos, Isliker, and Lepreti (2004) and Turkmani *et al.* (2005) and show promising results, but in our opinion the direct connection to solar flares is not yet entirely obvious.

Further possibilities are that the reconnection generated beams and/or the bulk outflow acts as a trigger for another acceleration mechanism like a fast mode termination shock (e.g., Somov and Kosugi, 1997; Tsuneta and Naito, 1998) or a collapsing magnetic trap (with or without a fast mode shock; e.g., Somov and Kosugi, 1997; Karlický and Kosugi, 2004). Last but not least, the reconnection outflow and/or the beams could generate favourable conditions for a turbulent cascade which leads to further stochastic acceleration in the way discussed by e.g. by Miller and co-workers (Miller and Roberts, 1995; Miller, LaRosa, and Moore, 1996; Lenters and Miller, 1998).

Acknowledgements

We would like to thank Paolo Giuliani, Alexandra Cran-McGreehin, Lyndsay Fletcher and the anonymous referee for useful comments. Paul Wood acknowledges financial support from a PPARC studentship.

References

Aschwanden, M.: 2002, *Particle Acceleration and Kinematics in Solar Flares*, Kluwer Academic Publishers, Drodrecht.
Browning, P. and Vekstein, G.: 2001, *J. Geophys. Res.* **106**, 18,677.
Bruhwiler, D. and Zweibel, E.: 1992, *J. Geophys. Res.* **97**, 10,825.
Bulanov, S. V. and Sasorov, P. V.: 1976, *Soviet Astron.* **52**, 763.
Craig, I. J. D. and Litvinenko, Y. E.: 2002, *Astrophys. J.* **570**, 387.
Drake, J. F., Swisdak, M., Cattell, C., Shay, M. A., Rogers, B. N., and Zeiler, A.: 2003, *Science* **299**, 873.
Fletcher, L. and Petkaki, P.: 1997, *Solar Phys.* **172**, 267.
Foukal, P. and Behr, B.: 1995, *Solar Phys.* **156**, 293.
Hamilton, B., McClements, K. G., Fletcher, L., and Thyagaraja, A.: 2003, *Solar Phys.* **214**, 339.
Harris, E. G.: 1962, *Nuovo Cimento* **23**, 115.
Heerikhuisen, J., Litvinenko, Y. E., and Craig, I. J. D.: 2002, *Astrophys. J.* **566**, 512.
Hesse, M.: 1995, in G. Klare (ed.), *Reviews of Modern Astronomy*, Vol. 8, Astronomische Gesellschaft, p. 323.
Hesse, M. and Schindler, K.: 1988, *J. Geophys. Res.* **93**, 5559.
Hesse, M., Kuznetsova, M., and Hoshino, M.: 2002, *J. Geophys. Res. Lett.* **29**, 4.
Holman, G., Sui, L., Schwartz, R., and Emslie, A.: 2003, *Astrophys. J.* **595**, L97.
Hurford, G., Schwartz, R., Krucker, S., Lin, R., Smith, D., and Vilmer, N.: 2003, *Astrophys. J.* **595**, L77.
Karlický, M. and Kosugi, T.: 2004, *Astron. Astrophys.* **419**, 1159.
Kliem, B.: 1994, *Astrophys. J.* **90**, 719.
Kliem, B., Karlický, M., and Benz, A. O.: 2000, *Astron. Astrophys.* **360**, 715.
LaRosa, T. N., Moore, R. L., Miller, J. A., and Shore, S. N.: 1996, *Astrophys. J.* **467**, 454.
Lenters, G. T. and Miller, J. A.: 1998, *Astrophys. J.* **493**, 451.
Lin, R., Mewaldt, R., and Hollebeke, M. V.: 1982, *Astrophys. J.* **253**, 949.
Litvinenko, Y.: 1996, *Astrophys. J.* **462**, 997.

Litvinenko, Y.: 2003, *Solar Phys.* **216**, 189.
Litvinenko, Y. and Craig, I.: 2000, *Astrophys. J.* **544**, 1101.
Litvinenko, Y. and Somov, B.: 1993, *Solar Phys.* **146**, 127.
Martens, P.: 1988, *Astrophys. J.* **330**, L131.
Martens, P. C. H. and Young, A.: 1990, *Astrophys. J. Suppl.* **73**, 333.
Metcalf, T. R., Alexander, D., Hudson, H. S., and Longcope, D. W.: 2003, *Astrophys. J.* **595**, 483.
Miller, J. and Roberts, D.: 1995, *Astrophys. J.* **452**, 912.
Miller, J., LaRosa, T., and Moore, R.: 1996, *Astrophys. J.* **461**, 445.
Miller, J., Cargill, P., Emslie, A., Holman, G., Dennis, B., LaRosa, T., Winglee, R., Benka, S., and Tsuneta, S.: 1997, *J. Geophys. Res.* **102**, 14,631.
Moore, R. L., LaRosa, T. N., and Orwig, L. E.: 1995, *Astrophys. J.* **438**, 985.
Nodes, C., Birk, G. T., Lesch, H., and Schopper, R.: 2003, *Phys. Plasmas* **10**, 835.
Northrop, T.: 1963, *The Adiabatic Motion of Charged Particles*, Interscience.
Petkaki, P. and Mackinnon, A.: 1997, *Solar Phys.* **172**, 279.
Priest, E. and Forbes, T. (eds.): 2000, 'Magnetic Reconnection: MHD Theory and Applications, Cambridge University Press, Cambridge.
Pritchett, P. and Coroniti, F.: 2004, *J. Geophys. Res.* **109**, A01220.
Ricci, P., Lapenta, G., and Brackbill, J. U.: 2003, *Phys. Plasmas* **10**, 3554.
Rogers, B. N., Drake, J. F., and Shay, M. A.: 2000, *J. Geophys. Res. Lett.* **27**, 3157.
Schindler, K., Hesse, M., and Birn, J.: 1991, *Astrophys. J.* **380**, 293.
Schopper, R., Birk, G., and Lesch, H.: 1999, *Phys. Plasmas* **6**, 4318.
Shay, M., Drake, J., Swisdak, M., Dorland, W., and Rogers, B.: 2003, *Geophys. Res. Lett.* **30**, 1345.
Somov, B. and Kosugi, T.: 1997, *Astrophys. J.* **485**, 859.
Tsuneta, S. and Naito, T.: 1998, *Astrophys. J.* **495**, L67.
Turkmani, R., Vlahos, L., Galsgaard, K., Cargill, P. J., and Isliker, H.: 2005, *Astrophys. J. Lett.* **620**, L59.
Vlahos, L., Isliker, H., and Lepreti, F.: 2004, *Astrophys. J.* **608**, 540.
Zeiler, A., Biskamp, D., Drake, J., Rogers, B., Shay, M., and Scholer, M.: 2002, *J. Geophys. Res.* **107**, 1230.
Zharkova, V. V. and Gordovskyy, M.: 2004, *Astrophys. J.* **604**, 884.